Research Article | Vol. 27, No. 12 | 10 Jun 2019 | OPTICS EXPRESS 17262

Optics EXPRESS

Study of crystalline defect induced optical scattering loss inside photonic waveguides in UV–visible spectral wavelengths using volume current method

HONG CHEN, HOUQIANG FU, JINGAN ZHOU, XUANQI HUANG, TSUNG-HAN YANG, KAI FU, CHEN YANG, JOSSUE A. MONTES, AND YUJI ZHAO*

School of Electrical, Computer and Energy Engineering, Arizona State University, Tempe, AZ 85287, USA

*yuji.zhao@asu.edu

Abstract: In this work, we study the crystalline defect induced optical scattering loss inside photonic waveguide. Volume current method is implemented with a close form of dyadic Green's function derived. More specifically, threading dislocation induced scattering loss inside AlN waveguides in UV–visible spectrum wavelengths are studied since this material is intrinsically accompanied with high densities of dislocations (typically on order of 10^8–10^{10}cm^{-2}). The results from this study reveal that threading dislocations contribute significant amount of scattering loss when material is not MOCVD grown. Additionally, the scattering loss is strongly dependent on polarization and waveguide geometries: TM modes exhibit higher scattering loss compared with TE modes, and the multimode large core waveguides are more susceptible to threading dislocations compared with single mode waveguides and high-aspect-ratio waveguides. Conclusions from this work can be supported by several recently published investigations on III-N based photonic devices. The model derived from this work can also be easily altered to fit other material systems with other types of crystalline defects.

1. Introduction

III-nitride (III-N) based integrated photonic waveguides (WGs) and resonators have enabled a wide variety of applications including modulators [1], harmonic generations [2,3], comb generations [4,5], quantum emitters [6,7], and light-emitting diodes/lasers [8,9]. Due to its wide bandgap and active integration capability, recently III-nitrides have attracted growing attentions for applications in UV-visible spectrum regime [10–12]. For traditional WGs working at IR wavelengths, wave propagation losses are mainly contributed by sidewall scattering, and they can be reduced by implementing geometries [12] that minimize the overlap between modes and scattering non-idealities. This design strategy is feasible for most of WG materials such as SiN_x [12,13]. However, there is another complicating factor for III-N materials grown on foreign substrates such as sapphire: high defect densities. For example, the metalorganic chemical vapor deposition (MOCVD) grown III-N thin films on sapphire exhibit high density of threading dislocations (TDs) over 10^{19} cm^{-2} [14], and density of TDs will be even higher for sputtered films [15]. Therefore, for III-N WGs, in addition to the sidewall scattering loss, internal defect induced scattering loss is also be of crucial importance to WG performance. Furthermore, as Rayleigh's law suggests, the scattering cross-section is proportional to λ^{-4}, indicating that small non-idealities (crystalline defects) will cause higher scattering loss in UV-visible wavelengths than in IR wavelengths. Since III-N materials are commonly employed as light-emitting/WG materials in UV-visible spectrum, III-N optical devices are expected to be more vulnerable to defect induced scattering losses.

#361945 https://doi.org/10.1364/OE.27.017262
Journal © 2019 Received 7 Mar 2019; revised 8 May 2019; accepted 10 May 2019; published 5 Jun 2019

Optics EXPRESS

There are two main types of defect induced WG losses: absorption-related loss and scattering-related loss. Recent studies have revealed different loss mechanisms in III-N optical devices due to crystalline defects including defect absorption [16], anisotropic non-ideal wet etching [17], free carrier absorption [18], and two-photon absorption [18]. However, the internal defect induced scattering loss is still not clear in these devices and demands rigorous investigations due to its significance in III-N WGs. In this work, we propose a semi-analytical method based on the volume current model (VCM) to calculate optical scattering losses from defects in AlN WGs. In comparison with previous models and analysis [19], in which the analysis was made within the scenario of point defects scattering in homogeneous medium, this work considered complex defect geometries and WG optical confinements. The model is ready to be applied to other III-N materials (GaN, AlGaN), if different index settings are utilized accordingly. The obtained results will be compared with other defect related loss mechanisms, and with previous experimental results.

This work is organized as following: in section 2, the numerical method implemented in this work will be presented. In section 3.1, the scattering properties of a single threading dislocation will be shown; additionally, in section 3.2, we extent the discussion into the loss properties of a more practical case where threading dislocation arrays will be considered. The TD induced scattering loss will be compared with sidewall scattering loss and discussions will be made. In section 4, we compare the scattering induced loss with other defect related loss mechanisms, and the limitation of this model will also be discussed. We will conclude this work in section 5.

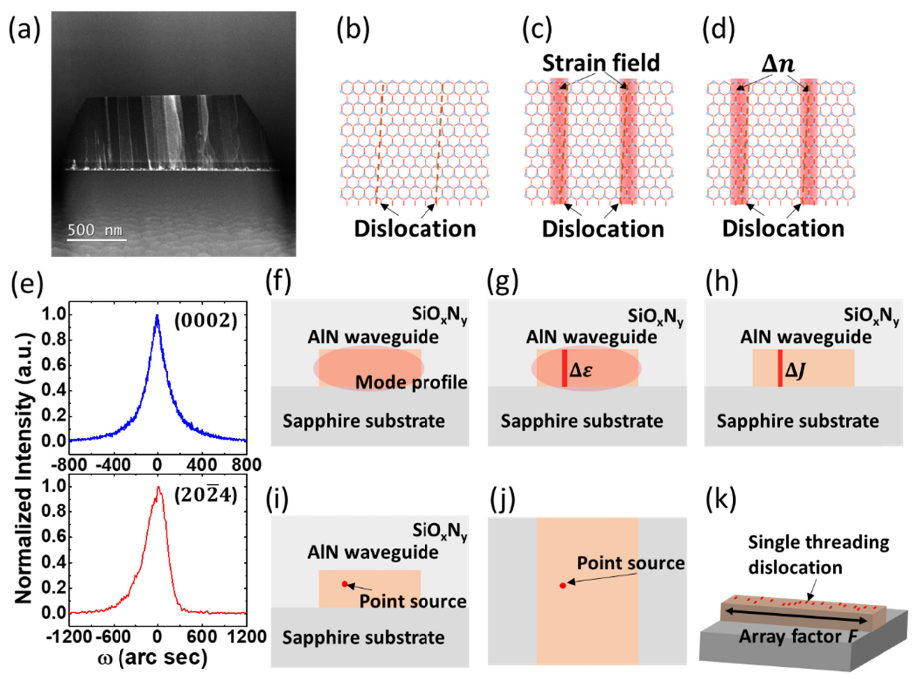

Fig. 1. (a) TEM cross-section image of AlN WGs. (b)–(d), the dielectric equivalent of threading dislocation for scattering analysis, see main text for detailed description. (e) Typical XRD data of AlN thin film grown on sapphire substrate by MOCVD, the threading dislocation density can be estimated using Eqs. (1) and (2). (f)–(k), the procedures to obtain the threading dislocation induced optical scattering loss, detailed description can be found in main text.

2. Methods

The transmission electron microscopy (TEM) image and AlN WG is depicted in Fig. 1(a). The AlN film was grown on sapphire substrates by MOCVD, where trimethylaluminum

(TMAl) and ammonia (NH_3) were used as precursors for Al and N, respectively. The details about the fabrication process of AlN WGs can be found elsewhere [10–12]. High density of TDs along c-axis can be clearly observed in AlN as shown in Fig. 1(a). It should be noted that the defect considered in this work is TD due to its large population in III-N. Other types of defects such as point defects and grain boundaries can also be analyzed using the proposed model. In this work, VCM is implemented to analyze the scattering properties [13,20]. A closed form of dyadic Green's function is derived for far-field response of point source excitation inside WG. This dyadic Green's function is implemented together with proper array factor [20] to estimate TD induced scattering loss inside AlN WGs. The model proposed in this research can be easily converted for different types of defects in different material systems. To model TD induced scattering loss properly, the distribution of TDs should be converted into a corresponding dielectric distribution, which in turn determines the scattering objectives. This task can be accomplished by making the following physical approximations. In the vicinity of TDs, the abnormal atom arrangements [Fig. 1(b)] result in strain fields near its neighboring sites [Fig. 1(c)]. This in turn leads to the photoelastic effect that causes a change of permittivity $\Delta\varepsilon$ and thus Δn as indicated in Fig. 1(d). According to [19], $|\Delta\varepsilon| = 2$ can be served as a typical order-of-magnitude estimate.

In this work, for simplicity, TDs are modeled by randomly (but with a correlation in between) distributed cylinders that perpendicular c-plane of sapphire substrate. Although the dimensions of TDs' cross-sections are in atomic scale, the strain field can extend to its neighboring sites, resulting in a lager effective cross-section. In this work, we assume that the radius of each "cylinder" is 0.5 nm [21]. The density of TD with screw (N_s) and edge (N_E) types can be estimated bawd on the X-ray diffraction (XRD) rocking curves (RC) of AlN thin films on (0002) plane and $(20\overline{2}4)$ plane using Eqs. (1) and (2), respectively, where β is the full-width-half-maximum (FWHM), b is the length of Burger's vector [22,23]. A typical XRD RC of AlN thin film grown by MOCVD is shown in Fig. 1(e), in which the FWHM of (0002) and $(20\overline{2}4)$ RCs are 194.1 and 313.8 arc sec, respectively, corresponding to TD density on order of of $\sim 10^8$ cm^{-2}.

$$N_S = \frac{\beta_S^2}{4.35|b_S|^2} \tag{1}$$

$$N_E = \frac{\beta_E^2}{4.35|b_E|^2} \tag{2}$$

The VCM is utilized to compute scattering loss contributed by TDs, a method commonly used in the analysis of sidewall scattering loss in WGs [13,20]. Since the dyadic Green's function associated with VCM derived in this work has a different format compared with previous studies [13,20], the derivation of VCM will be briefly revisited for complicity. To investigate the scattering loss in dB/cm, the first step is to compute modes within optical WG [Fig. 1(f)]. More specifically, the WG geometry in this study is AlN grown/sputtered on sapphire [5,10,11], and the cladding layer is SiO_xN_y deposited by plasma-enhanced chemical vapor deposition (PECVD) in order to match the refractive index of sapphire [10]. The index changes consequent from TDs can be considered as a weak perturbation, and the field distribution of modes is assumed to be almost unaltered. To satisfy wave equation, the change in refractive index will contribute a volume current density at the same location as shown in Figs. 1(g) and 1(h). According to [20], the amplitude of this volume current density $\vec{J}$ is governed by:

$$\vec{J}(\vec{r}) = -i\omega\Delta\varepsilon(\vec{r})\vec{E}(\vec{r}) \tag{3}$$

Optics EXPRESS

where ω is the photon angular frequency, $\Delta\varepsilon$ is the change of permittivity, $\vec{E}$ is the field intensity obtained by solving WG modes. The loss from a single TD can be analyzed by calculating the radiated power from this volume current source by dyadic Green's function. The dyadic Green's function in the far-field can be analytically derived by implementing method of stationary phase in two dimensions given by Eqs. (4) and (5), where intermedium components are given by Eqs. (6)–(14). $\overline{G}_{21}$ ($\overline{G}_{23}$) indicates the dyadic Green's function when source is located within medium 2 and the field point in medium 1(3). $\overline{G}_{11}$ and $\overline{G}_{13}$ are the dyadic Green's functions when the point source is located at the sidewall, formats of $\overline{G}_{11}$ and $\overline{G}_{13}$ can be found in [13] and [20]. Although Eqs. (4) and (5) are originally derived in this work, to keep it consistent with previous studies on sidewall scattering, all notations in Eqs. (4)–(14) are kept the same as [20].

$$\overline{G}_{21}\left(\vec{r}_c,\vec{r}_c^{\,'}\right)\approx\frac{e^{i\vec{k}_{1+,0}\bullet\left(\vec{r}_c-\vec{r}_c^{\,'}\right)}k_{1zc,0}^2\left[\overline{C}_M\dfrac{A^{TE}}{M_2^{TE}}+\overline{C}_{Np}\dfrac{A^{TM}}{M_2^{TM}}\right]e^{i\left(k_{1zc,0}-k_{2zc,0}\right)d_1}}{4\pi\left(z_c-z_c^{'}\right)k_1\left|k_{s0}\right|^2k_{2zc,0}} \tag{4}$$

$$\overline{G}_{23}\left(\vec{r}_c,\vec{r}_c^{\,'}\right)\approx-\frac{e^{i\vec{k}_{3-,0}\bullet\left(\vec{r}_c-\vec{r}_c^{\,'}\right)}k_{3zc,0}^2\left[\overline{C}_M\dfrac{B^{TE}}{M_2^{TE}}+\overline{C}_{Nm}\dfrac{B^{TM}}{M_2^{TM}}\right]e^{-i\left(k_{3zc,0}-k_{2zc,0}\right)d_2}}{4\pi\left(z_c-z_c^{'}\right)k_3\left|k_{s0}\right|^2k_{2zc,0}} \tag{5}$$

$$A^{TE}=\left[e^{i\left(k_{1zc,0}-k_{2zc,0}\right)z_c^{'}}+e^{ik_{2zc,0}\left(z_c^{'}+2d_2\right)+ik_{1zc,0}z_c^{'}}\hat{R}_{23}^{TE}\right]\hat{T}_{21}^{TE} \tag{6}$$

$$A^{TM}=\left[e^{i\left(k_{1zc,0}-k_{2zc,0}\right)z_c^{'}}+e^{ik_{2zc,0}\left(z_c^{'}+2d_2\right)+ik_{1zc,0}z_c^{'}}\hat{R}_{23}^{TM}\right]\hat{T}_{21}^{TM} \tag{7}$$

$$B^{TE}=\left[e^{-i\left(k_{3zc,0}-k_{2zc,0}\right)z_c^{'}}+e^{-ik_{2zc,0}\left(z_c^{'}+2d_1\right)-ik_{3zc,0}z_c^{'}}\hat{R}_{21}^{TE}\right]\hat{T}_{23}^{TE} \tag{8}$$

$$B^{TM}=\left[e^{-i\left(k_{3zc,0}-k_{2zc,0}\right)z_c^{'}}+e^{-ik_{2zc,0}\left(z_c^{'}+2d_1\right)-ik_{3zc,0}z_c^{'}}\hat{R}_{21}^{TM}\right]\hat{T}_{23}^{TM} \tag{9}$$

$$\overline{C}_{Np}=\left[\vec{k}_{n+}\times\left(\vec{k}_s\times\vec{z}_c\right)/k_n\right]\left[\vec{k}_{m-}\times\left(\vec{k}_s\times\vec{z}_c\right)/k_m\right] \tag{10}$$

$$\overline{C}_{Nm}=\left[\vec{k}_{n-}\times\left(\vec{k}_s\times\vec{z}_c\right)/k_n\right]\left[\vec{k}_{m+}\times\left(\vec{k}_s\times\vec{z}_c\right)/k_m\right] \tag{11}$$

$$\overline{C}_M=\left(\vec{k}_s\times\vec{z}_c\right)\left(\vec{k}_s\times\vec{z}_c\right) \tag{12}$$

$$M_2^{TE}=\left[1-R_{23}^{TE}R_{21}^{TE}e^{2ik_{2zc}\left(d_2-d_1\right)}\right]^{-1} \tag{13}$$

$$M_2^{TM}=\left[1-R_{23}^{TM}R_{21}^{TM}e^{2ik_{2zc}\left(d_2-d_1\right)}\right]^{-1} \tag{14}$$

The electric field can be computed using Eq. (15) when dyadic Green's function is obtained using Eqs. (4)–(14). The total radiated power can be obtained by integrating the Poynting vector in the far-field, where the ensemble average of Poynting vector in the far-field is given by Eq. (16).

$$\vec{E}\left(\vec{r}_c\right)=i\omega\mu\iiint\overline{G}\left(\vec{r}_c,\vec{r}_c^{\,'}\right)\bullet\vec{J}\left(\vec{r}_c^{\,'}\right)\mathrm{d}V' \tag{15}$$

$$P=\oint\!\!\!\oint\vec{S}\bullet\vec{r}\,\mathrm{d}A \tag{16}$$

Optics EXPRESS

To calculate the ensemble average of far-field Poynting vector, the same array factors can be implemented as [13] given by Eqs. (17) and (18), where σ is the equivalent roughness, L_c is the correlation length, and Ω is the spatial frequency. The scattering objective is assumed to be locating at the radiation location where average radiated power is obtained. The effective roughness σ^2 can be obtained by multiplying dislocation density ($D.D$) in cm^{-2} with WG width in the unit of μm.

$$\tilde{R}(\Omega) \approx \frac{2\sigma^2 L_c}{1 + L_c^2 \Omega^2} \tag{17}$$

$$\frac{P_{rad}}{L} = \int_0^{2\pi}\int_0^{\pi} (\vec{S}\bullet\vec{r})\,\tilde{R}(\beta - k_0 n_{cladd}\vec{r}\bullet\vec{z})\,r^2 \sin\theta d\theta d\phi \tag{18}$$

$$\sigma^2 = D.D.\times W \times 10^{-11} \tag{19}$$

The spatial distribution correlation of TDs inside III-N materials have been investigated by different groups, and the correlation length is varied from 50 nm [24] to a few microns [25]. The correlation length has weak influence on the scattering loss when it's sufficiently large [20]. Therefore, for simplicity, the correlation length used in this work is set as 100 nm.

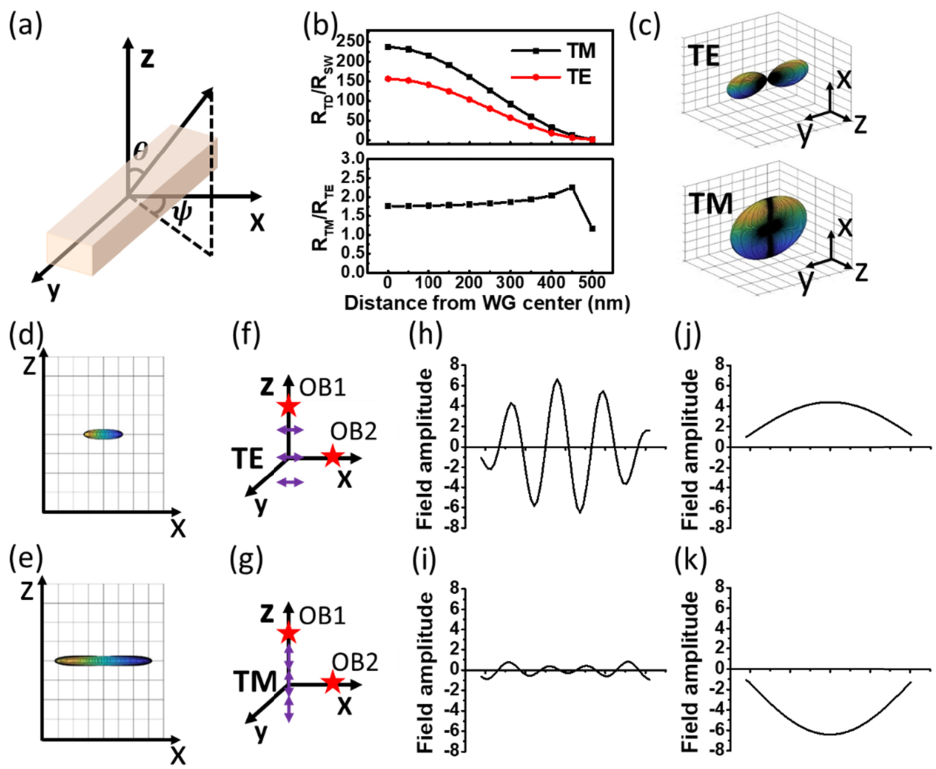

Fig. 2. (a) Coordinate system implemented in this study. (b) Threading dislocation scattered power versus sidewall non-ideality scattered power R_{TD}/R_{SW} for TE and TM mode, and the scattered power ratio between TM and TE mode R_{TM}/R_{TE}, when no WG confinement is considered. (c) Far-field power distribution of the scattered field for TE and TM excitation. (d), (e) WG cross-section view of scattered power distribution for TE and TM mode, respectively. (f), (g) Schematic for the dipole arrangement and OB points for TE and TM modes, respectively. (h)–(k) Field intensity versus dipole location for TE and TM dipoles at different observation points.

3. Results and discussions

3.1 Scattering properties of single threading dislocation

Prior to the investigations on scattering properties of TDs inside WGs, it is beneficial to initiate the discussion on the scattering properties of TDs inside a homogenous medium. Figure 2(a) depicts the coordinate system used in this work, in which the wave is propagating along y-direction and the thin film layer is grown along z-direction. Sidewall of waveguide is supposed to be defined by dry etching processes perpendicular to x-direction. More specifically, the z-direction corresponds to c-axis of AlN (or GaN) and sapphire. Under same excitation condition, the ratio between TD/sidewall scattered power and TE/TM scattered power versus TD location (x-axis) are shown in Fig. 2(b). A noteworthy feature is that TM excitation is intrinsically more radiative than TE excitation, indicating higher scattering loss from TM modes. The maximum scattered power of TDs are ~140 and ~60 times higher than sidewall for TM and TE modes, respectively, as the field intensity decays from the center. The significant difference between TM/TE scattered power can also be verified by their far-field distribution in Fig. 2(c), where the far-field pattern can be well understood by combining anisotropic dipole radiation [20] with linear dipole array theory [26].

One of the most important features obtained from this configuration is the highly anisotropic scattering property. Figures 2(d) and 2(e) show the far-field distribution in x-z plane for TE and TM modes, respectively. For TE modes, the radiated power along x-direction is ~5 times higher than that along z-direction for TE mode and for TM mode it is ~15 times higher. To explain this strong anisotropy, two observation (OB) points can be placed at z-axis and x-axis in the far-field as shown in Figs. 2(f) and 2(g). Figures 2(h)–2(k) show the field amplitude for each individual point source location in TE/TM modes. For OB point at z-axis, field amplitude is oscillating due to the phase difference between dipoles at different locations. Therefore, the total radiated power of "linear array" is minimized as the contribution from individual dipoles canceled each other. While for OB point at x-axis, in the far field, each dipole exhibits nearly identical phase. Therefore, the total radiated power of array is maximized. Noting that the dyadic Green's function only allows the existence of one pair of WG boundaries [20], it's feasible to keep the sidewall and omit the upper and lower boundaries [20], since most of the scattered power interacts with boundaries vertical to x-axis. Section 4 will discuss more about this assumption and possible limitations.

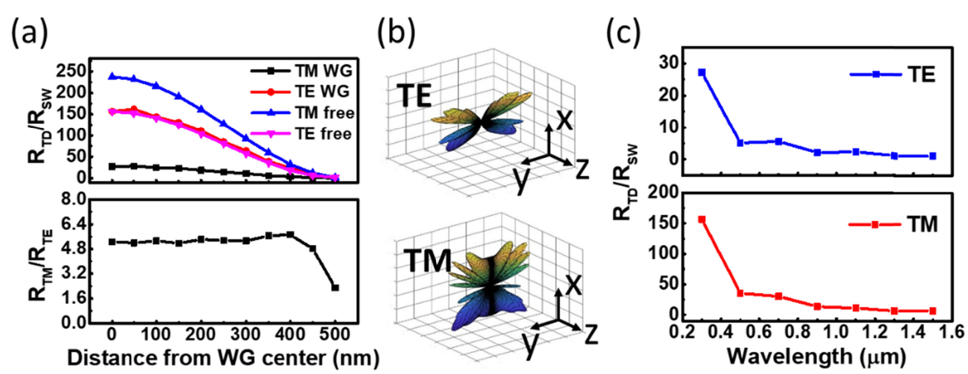

Fig. 3. (a). Threading dislocation scattered power versus sidewall non-ideality scattered power R_{TD}/R_{SW} for TE and TM mode, and the scattered power ratio between TM and TE mode R_{TM}/R_{TE}, when WG confinement is implemented. (b) The wavelength dependence of scattered power ratio. (c) Far-field power distribution of TE and TM excitation with WG confinement effect.

Figure 3 shows the scattering properties with WG confinement of a single TD by activating one pair of boundaries vertical to x-axis. R_{TD}/R_{SW} for TE/TM modes and power ratio between TE/TM modes for different locations of TDs are shown in Fig. 3(a). Due to the waveguiding effect, the scattered power becomes smaller with optical confinement as part of scattered power will be guided within WGs. Scattered power ratio between TM and TE mode is also higher than homogeneous situation in Fig. 2(b). This is because most of the TE scattered power is directed towards y-axis in guided mode. On the other hand, for TM mode, significant amount of scattered power travels along x-axis interacting with sidewall, leading to a ~10 times higher scattered power than TE mode at the WG center. Figure 3(b) depicts the far-field pattern of scattered power. Compared with Fig. 2(c), the field in y direction disappears due to the waveguiding effect, and the amplitude oscillation can be observed along x-axis due to constructive/deconstructive interferences from two WG boundaries. Figure 3(c) shows R_{TD}/R_{SW} as a function of wavelength. The ratio decreases with increasing wavelength, indicating that TDs induced scattering loss becomes more significant in short wavelength region.

Results from Fig. 3 can provide two important takeaways for real applications. Firstly, for a wide variety of nonlinear optical applications, controlled anomalous dispersion is required [4,5]. TM mode exhibits better dispersion properties under certain circumstances [4], especially for those applications in highly dispersive region. Since TM modes are more vulnerable to TDs, high material quality is of crucial importance in III-N optical devices, which in turn requires good epitaxial growth by MOCVD. Secondly, for the applications of harmonic generation [2,3], parametric conversion [27], supercontinuum generation [28], and comb generation, the spectrum can be as broad as one or several octaves, which may result in a large optical loss difference between IR and UV-visible light. This has been supported by many recent studies on AlN based optical devices and will be discussed more in session 4.

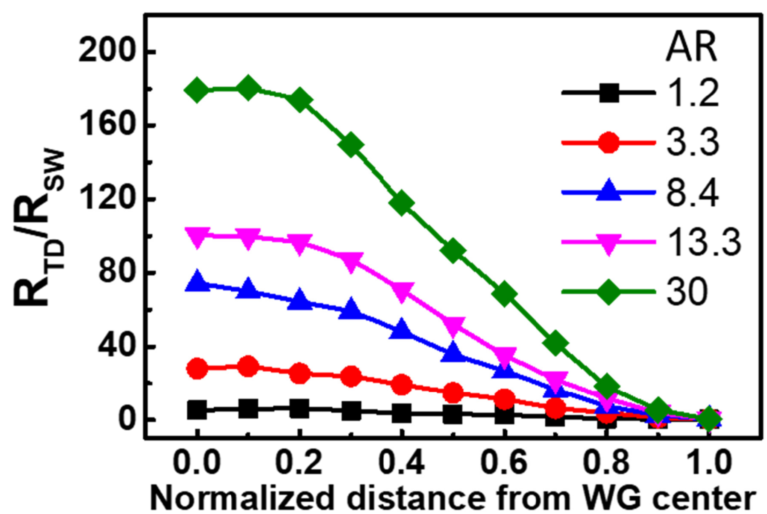

Fig. 4. The scattered power ratio R_{TD}/R_{SW} for HAR WGs at different aspect ratios.

In addition to normal WG geometries, the "high-aspect-ratio" (HAR) design has recently received growing attentions due to its capability of reducing sidewall scattering loss [13]. HAR design stretches the mode profile in the lateral dimension, which in turn minimizes the interaction between modes and sidewall impurities with single mode properties maintained. Propagation loss as low as 0.1 dB/m has been reported [13] using SiN WGs on SiO_2. For III-N materials, material quality becomes worse with reducing film thickness, which result in poor surface roughness [29]. Although traditional bottom-up approach cannot satisfy the surface roughness requirement to make III-N HAR WGs, it's still possible to tackle this problem by up-bottom approaches using selective wet etching [2]. Figure 4 shows the R_{TD}/R_{SW} versus TD location at different aspect ratio. When increasing the aspect ratio (AR) from 1.2 to 30, R_{TD}/R_{SW} increases from ~5.5 to ~650, the increasing R_{TD}/R_{SW} can be well understood by noting that R_{SW} is rapidly reduced by increasing AR, while the TDs are inside WGs thus exhibit weak geometry dependence, which result in weak dependence of R_{TD} on AR, therefore, R_{TD}/R_{SW} increases rapidly as the AR increases. The result shown in Fig. 4 also suggests that the performance of HAR WG exhibits strong material quality dependence.

3.2 Threading dislocation array induced optical scattering loss

The loss in dB/cm can be obtained by applying an array factor given in section 2. Figures 5(a) and 5(b) show the contour plots of optical loss parameters versus waveguide dimensions for TE and TM mode, respectively. The loss in dB/cm can be obtained by multiplying the loss parameters with $\sigma^2 \times \Delta\varepsilon^2$. Higher loss can be observed for TM mode, which is consistent with the conclusion in section 3.1. The minimum scattering loss is obtained in the HAR region, and the optical loss is reduced by reducing WG height. This is because the enhanced optical confinement in vertical direction squeezes the mode outside WG, and thus reduces the effective current density in TDs and the optical loss. Such observation is similar to the "squeeze out region" defined in [13]. When WG size becomes small in both dimensions (in the bottom-left corner), minimum loss can also be obtained, but the mode is squeezed in both vertical and lateral directions. It is also worth mentioning that TM modes exhibits weaker width dependence comparing with TE modes. The physical mechanism is that when the width increases, more scattered power from TE modes can be guided by WGs, leading to a smaller scattering loss. However, for TM mode, the scattered power is largely directed towards sidewall, and the scattering loss cannot be significantly reduced even with the enhanced waveguiding effect.

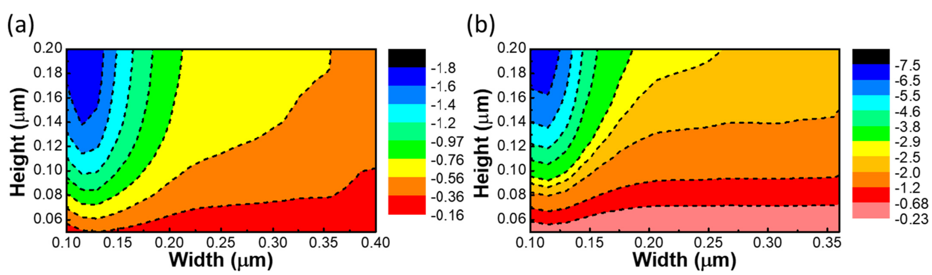

Fig. 5. (a) The loss map for TD induced scattering loss for TE mode excitation. (b) Same plot for TM mode excitation.

Based on previous discussions, six important WG designs are proposed and compared, whose WG dimensions and typical applications are also summarized in Table 1. Figures 6(a)–6(b) show the ratio between the TD scattering loss and the total loss, and the total loss in dB/cm for the six cases, respectively. Typical TD densities by different growth methods are provided in Table 2. For MOCVD grown devices, TDs contribute to a scattering loss less than 10%, this is supported by recent report on AlN high Q resonator in UV spectrum [11]. When the AlN is sputtered on sapphire substrates with a subsequent annealing process, a higher TD density can be expected, which can lead to higher TD induced optical losses. The typical annealing temperature for AlN on sapphire is above 1000°C [30]. These high temperatures are unacceptable especially when WGs are fabricated at the back-end of process flow. The annealing step (or MOCVD re-growth) itself can deteriorate or destroy other electronic or active optical devices. As a result, in some applications, sputtering without annealing is more realistic, where the TD densities are expected to be even higher and the loss is going to be larger. Another noteworthy scenario is the AlN sputtered on SiO_2, which has the potential to

Optics EXPRESS

be CMOS compatible [31]. However, due to the lack of crystalline arrangement, it's difficult to use TD density to describe the abundancy of defects. As it's reported in [4,5], a brute estimation on TD density is 10^{11}–10^{12} cm^{-2} according to Eqs. (1) and (2), but one should keep in mind that real defect density will be more excessive, because of the contribution from point defects and grain boundaries. Therefore, the total defect induced scattering losses will be even higher than what we estimated from this model.

Table 1. Six notable WG designs and their corresponding geometries.

Case	WG design	Width (μm)	Height (μm)	Typical application
1	Single mode, TE	0.2	0.1	Modulators, interferometers, sensors
2	Single mode, TM	0.2	0.1	
3	High aspect ratio	0.4	0.05	Low loss waveguides, high Q resonators
4	High aspect ratio	0.8	0.025	
5	Large core, TE	1	0.5	Low loss waveguides, high Q resonators
6	Large core, TM	1	0.5	

In short, TM modes are more vulnerable to TD induced loss. Traditional single mode WG geometry shows good tolerance to TDs but the total loss is high in UV region. This means that such geometry might not be a good candidate for real applications, which are consistent with previous reports from [5,10,11]. HAR WGs and large core WGs show better performance in terms of their total losses but also exhibit stronger dependences on TD density. Therefore, for single mode applications in short wavelengths, HAR design is more competitive compared with traditional single mode WG geometry. However, as a trade-off, III-N HAR design would require a top-down approach, which demands complicated fabrication processes. For other high Q resonator applications [2–5,7] (quantum optics, nonlinear optics), large core multimode WGs are required, in which the WG geometry has the strongest dependence on crystalline quality, and thus requires good MOCVD growth.

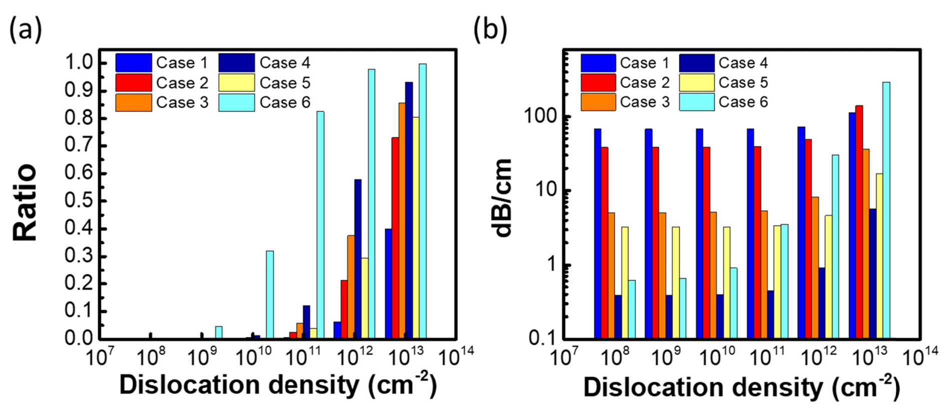

Fig. 6. (a) The ratio between TD induced scattering loss and total loss versus dislocation density for six noteworthy WG designs. (b) The total loss in dB/cm versus dislocation density.

Table 2. Typical dislocation density for AlN thin film grown by different methods

Epi-structure	Dislocation density (cm^{-2})
AlN grown on sapphire by MOCVD	10^8-10^9
AlN sputtered on sapphire (w. annealing)	~10^{10}
AlN sputtered on SiO_2 (w. annealing)	~10^{11}-10^{12}
AlN sputtered on SiO_2 (w/o. annealing)	>10^{13}

4. Other loss mechanisms and model validation

Since the loss estimation model proposed in this work is based on a scattering approach, active electron transitions (one/two photon absorption loss) are not involved. It's necessary to briefly investigate other loss mechanisms to clarify the applicable realistic scenarios of this model. Loss mechanisms that result in a positive imaginary part of refractive index are related to electron transitions, including free carrier absorption, one photon (defect) absorption, and two photon absorption.

As shown our previous report [18], free carrier loss can be well estimated by the Drude model. In GaN, the abundancy of nitrogen vacancies [32] provide large density of free carriers on order of 10^{18} [18], leading to a free carrier loss on order of 0.1–1 dB/cm depending on material qualities and operating wavelengths. In AlN, the free carrier density is several orders of magnitude lower than in GaN, which result in a negligibly free carrier loss. For defect absorptions [33], and [16] reported the absorptive detect levels for GaN and AlN, respectively. In GaN, deep energy levels contribute to electron transitions in the yellow spectral region [33]; while for AlN, multiple channels are present at the same time [16] including shallow donors (SD), Al vacancies, and O substitutions.

Then, the dominant defect related loss mechanisms will be discussed in GaN and AlN. In the long wavelength region, propagation loss in GaN is dominated by sidewall scattering and free carrier loss [18]. This observation is supported by numerous reports on GaN disk/ring resonators as their Q factors are capped on order of 10^4 [2]. In the short wavelength region, the losses are impacted by both the TD induced scattering loss and the free carrier loss, since a higher TD density is usually accompanied with a strong n-type conductivity [36].

However, free carrier loss is not the major loss mechanism in AlN due to the lack of conductivity. For MOCVD grown AlN WGs, in the short wavelength region, using the geometry parameters in a recent study [10] in UV-visible spectrum wavelength, by assuming L_c = 100 nm, the corresponding sidewall roughness is 3 nm, noting that the state-of-the-art ICP etching process can only provide a minimal roughness in this range, it is convincible to conclude that for MOCVD grown AlN, in the short wavelength, the dominated optical loss mechanism is still sidewall scattering, such conclusion can also be verified by another recent research activity on AlN ring resonator [11] where the Q factor can reach 10^5. For sputtered AlN, in the short wavelength, both defect absorption and defect induced scattering loss are important. As a result, the typical loss within this spectrum wavelength is on order of 15 dB/cm.

For MOCVD grown and sputter AlN WGs (or resonators), in the long wavelength region, the small photon energy is insufficient for electron transition between defect states, therefore, the influential mechanism is the TD induced scattering loss. The state-of-the-art MOCVD grown AlN ring resonator in IR exhibits intrinsic Q factor above 10^6, while the Q factors of sputtered AlN rings are in the range of mid 10^5 due to the large density of defects.

It also worth noting that regarding III-N disk resonators, the anisotropic wet etching during undercut process could lead to additional roughness, while for III-N WGs, the dry etching relies on physical bombardments thus exhibit less defect density dependence.

There are several limitations of this model. Firstly, only one pair of WG boundaries are involved in the scattering loss calculation. When height of WG approaches $\lambda / 2n$, the scattered power towards upper/lower boundaries increase. Consequently, the TD induced loss will be slightly higher than what we computed using this model. Additionally, other types of defects are not involved in this model, which leads to an underestimated optical loss. To improve this model, several advanced computing techniques can be employed. To compute the far-field distribution accurately, finite element method can be implemented [34], which requires intense computing. Moreover, a recently proposed model [35] allows the decomposition of guided mode and radiative mode, providing the opportunity to obtain the far-field with only near fields computed.

5. Conclusions

To conclude, we present a model to estimate optical scattering loss induce by TDs, the obtained results are compared with sidewall scattering loss. Several WG geometries in interests are investigated, where TM modes are more vulnerable to TDs, and the large core waveguide exhibits strongest performance dependence on material crystalline quality. The key conclusion is that MOCVD grown III-N materials provides excellent waveguiding performance while sputtered WGs exhibit strong defect induced scattering loss in the short wavelength region. This work reveals the importance of MOCVD growth to the application of III-N optical devices, it is also beneficial to the modeling on III-N WGs and other passive/active optical devices.

Funding

Army Research Office, W911NF-19-1-0089.

Acknowledgments

This research was monitored by Dr. Michael Gerhold. We gratefully acknowledge the use of facilities within the LeRoy Eyring Center for Solid State Science and CLAS Ultra-Fast Laser Facility at Arizona State University.

References

1. C. Xiong, W. H. Pernice, and H. X. Tang, "Low-loss, silicon integrated, aluminum nitride photonic circuits and their use for electro-optic signal processing," Nano Lett. **12**(7), 3562–3568 (2012).
2. C. Xiong, W. Pernice, K. K. Ryu, C. Schuck, K. Y. Fong, T. Palacios, and H. X. Tang, "Integrated GaN photonic circuits on silicon (100) for second harmonic generation," Opt. Express **19**(11), 10462–10470 (2011).
3. X. Guo, C. L. Zou, and H. X. Tang, "Second-harmonic generation in aluminum nitride microrings with 2500%/W conversion efficiency," Optica **3**(10), 1126–1131 (2016).
4. H. Jung and H. X. Tang, "Aluminum nitride as nonlinear optical material for on-chip frequency comb generation and frequency conversion," Nanophotonics **5**(2), 263–271 (2016).
5. X. Liu, C. Sun, B. Xiong, L. Wang, J. Wang, Y. Han, Z. Hao, H. Li, Y. Luo, J. Yan, T. Wei, Y. Zhang, and J. Wang, "Integrated High-Q Crystalline AlN Microresonators for Broadband Kerr and Raman Frequency Combs," ACS Photonics **5**(5), 1943–1950 (2018).
6. A. M. Berhane, K. Y. Jeong, Z. Bodrog, S. Fiedler, T. Schröder, N. V. Triviño, T. Palacios, A. Gali, M. Toth, D. Englund, and I. Aharonovich, "Bright Room-Temperature Single-Photon Emission from Defects in Gallium Nitride," Adv. Mater. **29**(12), 1605092 (2017).
7. M. Arita, F. Le Roux, M. J. Holmes, S. Kako, and Y. Arakawa, "Ultraclean single photon emission from a GaN quantum dot," Nano Lett. **17**(5), 2902–2907 (2017).
8. H. Sun, M. K. Shakfa, M. M. Muhammed, B. Janjua, K. H. Li, R. Lin, T. K. Ng, I. S. Roqan, B. S. Ooi, and X. Li, "Surface-passivated AlGaN nanowires for enhanced luminescence of ultraviolet light emitting diodes," ACS Photonics **5**(3), 964–970 (2018).
9. Y. Zhao, S. Tanaka, C. C. Pan, K. Fujito, D. Feezell, J. S. Speck, S. P. DenBaars, and S. Nakamura, "High-power blue-violet semipolar (2021) InGaN/GaN light-emitting diodes with low efficiency droop at 200 A/cm2," Appl. Phys. Express **4**(8), 082104 (2011).
10. T. J. Lu, M. Fanto, H. Choi, P. Thomas, J. Steidle, S. Mouradian, W. Kong, D. Zhu, H. Moon, K. Berggren, J. Kim, M. Soltani, S. Preble, and D. Englund, "Aluminum nitride integrated photonics platform for the ultraviolet to visible spectrum," Opt. Express **26**(9), 11147–11160 (2018).
11. X. Liu, A. W. Bruch, Z. Gong, J. Lu, J. B. Surya, L. Zhang, J. Wang, J. Yan, and H. X. Tang, "Ultra-high-Q UV microring resonators based on a single-crystalline AlN platform," Optica **5**(10), 1279–1282 (2018).
12. M. Stegmaier, J. Ebert, J. M. Meckbach, K. Ilin, M. Siegel, and W. H. P. Pernice, "Aluminum nitride nanophotonic circuits operating at ultraviolet wavelengths," Appl. Phys. Lett. **104**(9), 091108 (2014).
13. J. F. Bauters, M. J. Heck, D. John, D. Dai, M. C. Tien, J. S. Barton, A. Leinse, R. G. Heideman, D. J. Blumenthal, and J. E. Bowers, "Ultra-low-loss high-aspect-ratio Si3N4 waveguides," Opt. Express **19**(4), 3163–3174 (2011).
14. J. Bai, M. Dudley, W. H. Sun, H. M. Wang, and M. A. Khan, "Reduction of threading dislocation densities in AlN/ sapphire epilayers driven by growth mode modification," Appl. Phys. Lett. **88**(5), 051903 (2006).
15. C. Xiong, W. H. Pernice, X. Sun, C. Schuck, K. Y. Fong, and H. X. Tang, "Aluminum nitride as a new material for chip-scale optomechanics and nonlinear optics," New J. Phys. **14**(9), 095014 (2012).
16. G. Liu, C. Yan, G. Zhou, J. Wen, Z. Qin, Q. Zhou, B. Li, R. Zheng, H. Wu, and Z. Sun, "Broadband White-Light Emission from Alumina Nitride Bulk Single Crystals," ACS Photonics **5**(10), 4009–4013 (2018).
17. T. J. Puchtler, A. Woolf, T. Zhu, D. Gachet, E. L. Hu, and R. A. Oliver, "Effect of threading dislocations on the quality factor of InGaN/GaN microdisk cavities," ACS Photonics **2**(1), 137–143 (2015).
18. H. Chen, H. Fu, X. Huang, X. Zhang, T. H. Yang, J. A. Montes, I. Baranowski, and Y. Zhao, "Low loss GaN waveguides at the visible spectral wavelengths for integrated photonics applications," Opt. Express **25**(25), 31758–31773 (2017).
19. D. L. Mills, "Light scattering by point defects in insulating crystals," J. Appl. Phys. **51**(11), 5864–5867 (1980).

20. T. Barwicz and H. A. Haus, "Three-dimensional analysis of scattering losses due to sidewall roughness in microphotonic waveguides," J. Lit. Technol. **23**(9), 2719–2732 (2005).
21. Y. Tokumoto, S. I. Amma, N. Shibata, T. Mizoguchi, K. Edagawa, T. Yamamoto, and Y. Ikuhara, "Fabrication of electrically conductive nanowires using high-density dislocations in AlN thin films," J. Appl. Phys. **106**(12), 124307 (2009).
22. X. Huang, H. Fu, H. Chen, Z. Lu, I. Baranowski, J. Montes, T. H. Yang, B. P. Gunning, D. Koleske, and Y. Zhao, "Reliability analysis of InGaN/GaN multi-quantum-well solar cells under thermal stress," Appl. Phys. Lett. **111**(23), 233511 (2017).
23. H. Fu, I. Baranowski, X. Huang, H. Chen, Z. Lu, J. Montes, X. Zhang, and Y. Zhao, "Demonstration of AlN Schottky barrier diodes with blocking voltage over 1 Kv," IEEE Electron Device Lett. **38**(9), 1286–1289 (2017).
24. V. M. Kaganer and K. K. Sabelfeld, "X-ray Diffraction peaks from correlated dislocations: Monte Carlo study of dislocation screening," Acta Crystallogr. A **66**(6), 703–716 (2010).
25. V. S. Kopp, V. M. Kaganer, M. V. Baidakova, W. V. Lundin, A. E. Nikolaev, E. V. Verkhovtceva, M. A. Yagovkina, and N. Cherkashin, "X-ray determination of threading dislocation densities in GaN/Al2O3 (0001) films grown by metalorganic vapor phase epitaxy," J. Appl. Phys. **115**(7), 073507 (2014).
26. A. B. Constantine, "Antenna theory: analysis and design. MICROSTRIP ANTENNAS, third edition," John wiley & sons (2005).
27. X. Guo, C. L. Zou, C. Schuck, H. Jung, R. Cheng, and H. X. Tang, "Parametric down-conversion photon-pair source on a nanophotonic chip," Light Sci. Appl. **6**(5), e16249 (2016).
28. D. D. Hickstein, H. Jung, D. R. Carlson, A. Lind, I. Coddington, K. Srinivasan, G. G. Ycas, D. C. Cole, A. Kowligy, C. Fredrick, S. Droste, E. S. Lamb, N. R. Newbury, H. X. Tang, S. A. Diddams, and S. B. Papp, "Ultrabroadband supercontinuum generation and frequency-comb stabilization using on-chip waveguides with both cubic and quadratic nonlinearities," Phys. Rev. Appl. **8**(1), 014025 (2017).
29. S. B. Thapa, C. Kirchner, F. Scholz, G. M. Prinz, K. Thonke, R. Sauer, A. Chuvilin, J. Biskupek, U. Kaiser, and D. Hofstetter, "Structural and spectroscopic properties of AlN layers grown by MOVPE," J. Cryst. Growth **298**, 383–386 (2007).
30. H. Miyake, C. H. Lin, K. Tokoro, and K. Hiramatsu, "Preparation of high-quality AlN on sapphire by high-temperature face-to-face annealing," J. Cryst. Growth **456**, 155–159 (2016).
31. J. S. Levy, A. Gondarenko, M. A. Foster, A. C. Turner-Foster, A. L. Gaeta, and M. Lipson, "CMOS-compatible multiple-wavelength oscillator for on-chip optical interconnects," Nat. Photonics **4**(1), 37–40 (2010).
32. J. Neugebauer, C. G. Van de Walle, "Atomic geometry and electronic structure of native defects in GaN," Phys. Rev. B Condens. Matter **50**(11), 8067–8070 (1994).
33. T. Ogino and M. Aoki, "Mechanism of yellow luminescence in GaN," Jpn. J. Appl. Phys. **19**(12), 2395–2405 (1980).
34. C. Ciminelli, F. Dell'Olio, V. M. Passaro, and M. N. Armenise, "Fully three-dimensional accurate modeling of scattering loss in optical waveguides," Opt. Quantum Electron. **41**(4), 285–298 (2009).
35. J. Yang, J. P. Hugonin, and P. Lalanne, "Near-to-far field transformations for radiative and guided waves," ACS Photonics **3**(3), 395–402 (2016).
36. C. Gupta, Y. Enatsu, G. Gupta, S. Keller, and U. K. Mishra, "High breakdown voltage p–n diodes on GaN on sapphire by MOCVD," Phys. Status Solidi., A Appl. Mater. Sci. **213**(4), 878–882 (2016).